

1      **Turbulence Measurements from Compliant Moorings - Part II: Motion**

2      **Correction**

3      Levi F. Kilcher\*

4      *National Renewable Energy Laboratory, Golden, Colorado, USA*

5      Jim Thomson

6      *Applied Physics Laboratory, University of Washington, Seattle, Washington, USA*

7      Samuel Harding

8      *Pacific Northwest National Laboratory, Richland, Washington, USA*

9      Sven Nylund

10     *Nortek AS, Norway*

11    \*Corresponding author address: Levi Kilcher, National Renewable Energy Laboratory, 15013 Den-  
12    ver West Pkwy, Golden, Colorado, USA

13    E-mail: Levi.Kilcher@nrel.gov

## ABSTRACT

14      Acoustic Doppler velocimeters (ADVs) are a valuable tool for making high-  
15      precision measurements of turbulence, and moorings are a convenient and  
16      ubiquitous platform for making many kinds of measurements in the ocean.  
17      However, because of concerns that mooring motion can contaminate turbu-  
18      lence measurements and acoustic Doppler profilers make mid-depth veloc-  
19      ity measurements relatively easy, ADVs are not frequently deployed from  
20      moorings. This work demonstrates that inertial motion measurements can  
21      be used to reduce motion-contamination from moored ADV velocity mea-  
22      surements. Three distinct mooring platforms were deployed in a tidal channel  
23      with inertial-motion-sensor-equipped ADVs. In each case, motion correction  
24      based on the inertial measurements reduces mooring motion contamination of  
25      velocity measurements. The spectra from these measurements are consistent  
26      with other measurements in tidal channels, and have a  $f^{-5/3}$  slope at high  
27      frequencies—consistent with Kolmogorov’s theory of isotropic turbulence.  
28      Motion correction also improves estimates of cross spectra and Reynold’s  
29      stresses. Comparison of turbulence dissipation with flow speed and turbu-  
30      lence production indicates a bottom boundary layer production-dissipation  
31      balance during ebb and flood that is consistent with the strong tidal forcing  
32      at the site. These results indicate that inertial-motion-sensor-equipped ADVs  
33      are a valuable new tool for making high-precision turbulence measurements  
34      from moorings.

35 **1. Introduction**

36 Acoustic Doppler velocimeters (ADVs) have been used to make high-precision measurements  
37 of water velocity for over 20 years (Kraus et al. 1994; Lohrmann et al. 1995). During that time,  
38 they have been deployed around the world to measure turbulence in a range of environments and  
39 from a range of platforms, including the laboratory setting (Voulgaris and Trowbridge 1998), from  
40 stationary structures on ocean-, river- and lake-bottoms (Kim et al. 2000; Lorke 2007; Cartwright  
41 et al. 2009), in surface waters from a pole lowered from a ship's bow (Geyer et al. 2008), and in the  
42 deep ocean from autonomous underwater vehicles (e.g., Zhang et al. 2001; Goodman et al. 2006).

43 A relatively small fraction of ADV measurements have been made from moorings (e.g., Fer and  
44 Paskyabi 2014). Presumably this is because mooring motion can contaminate ADV measurements,  
45 and acoustic Doppler profilers (ADPs) can measure some mid-depth turbulence statistics without a  
46 mooring (e.g., Stacey et al. 1999a; Rippeth et al. 2002; Wiles et al. 2006; Guerra Paris and Thom-  
47 son 2017). Still, ADV measurements have distinct advantages: they are capable of higher sample  
48 rates, have higher signal-to-noise ratios, and have a much smaller sample volume (1 centimeter, as  
49 opposed to several meters).

50 Inertial motion unit (IMU) sensors have been used in the aerospace and aeronautical industries  
51 to quantify the motion of a wide range of systems, and to improve atmospheric velocity measure-  
52 ments, for several decades (Axford 1968; Edson et al. 1998; Bevly 2004). In the last decade, the  
53 smartphone, drone, and ‘Internet of Things’ markets have driven innovation in microelectrical-  
54 mechanical systems, including the IMU. As a result of this growth and innovation, the cost, power  
55 requirements, and size of IMUs have come down. These changes have allowed these sensors to be  
56 integrated into oceanographic instruments that have small form-factors, and rely on battery power.

57 Nortek now offers a version of their Vector ADV with a Microstrain 3DM-GX3-25 IMU sen-  
58 sor (Nortek 2005; MicroStrain 2012). This IMU's signals are incorporated into the Vector data  
59 stream so that its motion and orientation signals are tightly synchronized with the ADV's velocity  
60 measurements. The tight synchronization provides a dataset that can be utilized to quantify ADV  
61 motion in the Earth's inertial reference frame, and remove that motion from the ADV's velocity  
62 measurements at each time step of its sampling (Edson et al. 1998). This work utilizes 'ADV-IMU'  
63 measurements from mid-depth moorings in Puget Sound to demonstrate that motion correction can  
64 improve the accuracy of oceanic turbulence spectra, turbulence dissipation, and Reynolds stress  
65 estimates.

66 This effort was originally motivated by a need for low-cost, high-precision turbulence measure-  
67 ments for the emerging tidal energy industry (McCaffrey et al. 2015; Alexander and Hamlington  
68 2015). Experience in the wind energy industry has shown that wind turbine lifetime is related  
69 to atmospheric turbulence, and the same is expected to be true for tidal energy turbines. In the  
70 atmosphere, meteorological towers are often used to position sonic anemometers at the hub height  
71 of wind turbines for measuring detailed turbulence inflow statistics (Hand et al. 2003; Kelley et al.  
72 2005; Mücke et al. 2011; Afgan et al. 2013). In the ocean, tower-mounted hub-height turbulence  
73 measurements have been made, but they are challenging to install and maintain in energetic tidal  
74 sites (Gunawan et al. 2014; Thomson et al. 2012). Therefore, the U.S. Department of Energy  
75 funded this work to investigate the accuracy of mooring-deployed ADV-IMUs to reduce the cost  
76 of turbulence measurements at tidal energy sites (Kilcher et al. 2016). The approach proved to be  
77 successful and potentially useful to the broader oceanographic community interested in moored  
78 turbulence measurements (Lueck and Huang 1999; Doherty et al. 1999; Nash et al. 2004; Perlin  
79 and Moum 2012; Alford 2010; Paskyabi and Fer 2013).

80 The next section describes details of the measurements, including a summary of the hardware  
81 configurations (platforms) that were used to support and position the ADV-IMUs in the water  
82 column. A detailed description of the motion of these platforms is found in the companion paper  
83 to this work, Harding et al. (2017), hereafter Part 1. Section 3 describes the mathematical details  
84 of motion correction and Section 4 presents results from applying the method to measurements  
85 from the various platforms. Section 5 is a discussion of the energetics of the tidal channel in  
86 which the measurements were made and demonstrates that the measurements are consistent with  
87 turbulence theory and other measurements in similar regimes. A summary and concluding remarks  
88 are provided in Section 6.

## 89 **2. Measurements**

90 This work focuses on measuring turbulence from ADVs that are equipped with IMUs and de-  
91 ployed from moving (moored) platforms. The ADVs utilized for these measurements were Nortek  
92 Vector ADVs equipped with Microstrain 3DM-GX3-25 IMUs. These IMUs captured all six com-  
93 ponents of ADV motion (three components of angular rotation and three components of linear  
94 acceleration), as well as the orientation of the ADV pressure case. The IMU measures its motion  
95 at 1 kHz and uses internal signal integration (Kalman filtering) to output the motion signals at  
96 the same sample rate as the ADV's velocity measurements (the measurements are synchronized to  
97 within  $10^{-2}$  s). This reduces aliasing of the IMU's motion measurements above the ADV's sample  
98 rate (MicroStrain 2010).

99 All measurements used in this work were made in Admiralty Inlet, Washington, approximately  
100 500 m west southwest of Admiralty Head in 60 m of water at  $48^{\circ} 9.18' \text{ N}$ ,  $122^{\circ} 41.22' \text{ W}$  (Fig-  
101 ure 1). The site is approximately 6 km east of Port Townsend. Admiralty inlet is the largest  
102 waterway connecting Puget Sound to the Strait of Juan de Fuca, and it possesses a large semid-

103 iurnal tidal flow (Thomson et al. 2012; Polagye and Thomson 2013). This work utilizes data  
104 from three distinct deployment platforms: the tidal turbulence mooring, a StableMoor buoy, and  
105 a sounding weight. Each of these platforms are briefly described below, and additional details,  
106 photos, and schematic diagrams can be found in Part 1. All data and source files for this entire  
107 work—including manuscript latex source, figures, data downloading scripts, processing scripts,  
108 and analysis scripts—are publicly available.

109 *a. Tidal Turbulence Mooring*

110 The tidal turbulence mooring (TTM) is a simple mooring system with a strongback fin sus-  
111 pended between a steel clump-weight anchor weighing 1,200 kg when dry and a 0.93-m-diameter  
112 spherical steel buoy with a buoyancy of 320 kg. The ADV pressure cases were clamped to one  
113 side of the strongback fin and the ADV sensor head was positioned 10 cm in front of the fin’s  
114 leading edge (Figure 2). The leading edge of the fin is fastened inline with the mooring line. This  
115 configuration was designed to work like a weather vane, such that the drag on the fin held the ADV  
116 head upstream of the mooring components. This work utilizes data from two TTM deployments.

117 The first TTM deployment was from 1730 local time (LT) 12 June 2012 until 1430 LT 14 June  
118 2012. Two Nortek ADVs were clamped to either side of the fin so that the axis of their cylindrical  
119 pressure cases were parallel with the leading edge of the strongback. The ADV heads were spaced  
120 0.5 m apart vertically along the fin. Only one of these ADVs was equipped with an integrated  
121 IMU. This TTM also had an upward-looking ADP mounted on the mooring anchor.

122 Periods of time during which this mooring interfered with a beam of the ADP were identified  
123 by inspecting the profiler’s acoustic amplitude signal. Periods during which one beam of the  
124 profiler had  $> 5\%$  higher acoustic amplitude than the other beams were flagged as “contaminated”

<sup>125</sup> and excluded from averaging. Five-minute averages in which more than 50% of the data were  
<sup>126</sup> contaminated in this way were masked as invalid.

<sup>127</sup> The second TTM deployment was from 0600 LT 17 June 2014 to 0500 LT 19 June 2014. Two  
<sup>128</sup> Nortek ADV-IMUs were mounted on this TTM, with their heads spaced 0.5 m apart along the fin.  
<sup>129</sup> In this case, the pressure cases and ADV heads were inclined at an angle of 18° from normal to  
<sup>130</sup> the leading edge of the fin to account for mooring blowdown during strong currents (Figure 3).  
<sup>131</sup> This change was made to reduce vibrational motion observed during the June 2012 deployment  
<sup>132</sup> that was believed to be associated with the orientation of the pressure cases. There was no ADP on  
<sup>133</sup> the anchor of this TTM.

<sup>134</sup> *b. The StableMoor platform*

<sup>135</sup> The second deployment platform was a cylindrical, StableMoor™, syntactic foam buoy (man-  
<sup>136</sup>ufacturer: Deep Water Buoyancy) that was anchored to a clump weight that weighed 1,200 kg  
<sup>137</sup> (Figure 4). The buoy is 3.5 m long and 0.45 m in diameter with a tail ring that is 0.76 m in diame-  
<sup>138</sup>ter. The StableMoor buoy (hereafter, ‘SMB’) weighs 295 kg in air, and has a buoyancy of 185 kg  
<sup>139</sup> in water.

<sup>140</sup> The SMB was deployed with an ADV-IMU mounted at its nose from 11:21 on May 12 to 11:53  
<sup>141</sup> on May 13, 2015 (local time). The sample volume of the ADV is 10 cm forward of the nose and 20  
<sup>142</sup> cm above the center line of the SMB (Figure 4). Based on Wyngaard et al.’s (1985) investigation  
<sup>143</sup> of a similarly shaped slender body, the velocity measurements should have flow-distortion effects  
<sup>144</sup> of less than 10%. The SMB was equipped with a 1,200-kHz RDI workhorse sentinel ADP that  
<sup>145</sup> was oriented downward-looking to measure water velocity below the platform in twelve 1-m bins  
<sup>146</sup> and measure platform motion (“bottom tracking”), all at a 1-Hz sample rate.

147 The SMB has two primary advantages compared to the TTM. First, it is significantly more  
148 massive and hydrodynamically stable than the TTM, which reduces the frequency of motions of  
149 the platform (Part I). Second, the SMB is capable of supporting a bottom-tracking ADP, which  
150 provides an independent measure of the platform's translational motion. Disadvantages of the  
151 SMB include: its size, which adds to the challenge of deployment and recovery, and its cost,  
152 which is significantly higher than the TTM system.

153 *c. Turbulence Torpedo*

154 The turbulence torpedo is a simple sounding weight with an ADV head mounted forward of the  
155 nose, and the ADV pressure case strapped below (Figure 5). This platform was deployed on May  
156 14, 2015, for 37 minutes starting at 07:41 local time. This measurement was made from a davit  
157 that hung the system from the side of the ship to a depth of approximately 25 m. The primary  
158 advantages of this platform are its compact size, low cost, and the flexibility to perform spatial  
159 transects.

160 *d. Coordinate system and turbulence averaging*

161 Unless stated otherwise, vector quantities in this work are in a fixed “principal-axes” coordinate  
162 system that is aligned with the bidirectional tidal flow: positive  $u$  is in the direction of ebb ( $310^\circ$   
163 True), positive  $w$  is vertically upward, and  $v$  is the cross-stream component in a right-handed  
164 coordinate system (Figure 1). The full velocity vector,  $\tilde{\mathbf{u}} = (\tilde{u}, \tilde{v}, \tilde{w})$ , is separated into a mean and  
165 turbulent component as  $\tilde{\mathbf{u}} = \bar{\mathbf{u}} + \mathbf{u}$ , where the over-bar denotes a 5-minute average. Turbulence  
166 kinetic energy,  $tke = \overline{u^2} + \overline{v^2} + \overline{w^2}$ , and Reynold's stresses,  $\overline{uv}$ ,  $\overline{uw}$ ,  $\overline{vw}$ , are also estimated using  
167 a 5-minute average. The horizontal velocity magnitude is computed as,  $\bar{U} = (\bar{u}^2 + \bar{v}^2)^{1/2}$ . The  
168 friction velocity is estimated as,  $u_* = (\overline{uw^2} + \overline{vw^2})^{1/4}$ ; note that this is taken at the height of the

169 ADV measurements, and should therefore only be interpreted as a proxy for the friction velocity  
170 at the bottom boundary.

171 All spectra,  $S\{x\}(f) = |\mathcal{F}\{x(t)\}|^2$ , and cross spectra,  $C\{x,y\}(f) = \text{real}(\mathcal{F}\{x(t)\}\mathcal{F}\{y(t)\})$ , are  
172 computed using NumPy fast Fourier transform routines (van der Walt et al. 2011). Here,  $\mathcal{F}\{x(t)\}$   
173 denotes the fast Fourier transform of a signal  $x(t)$  that has been linearly detrended and Hanning  
174 windowed to reduce spectral reddening.

175 Throughout the remainder of this work, the dependence of  $S$  and  $C$  on  $f$  is implied (e.g.,  $S\{x\}(f)$   
176 is hereafter  $S\{x\}$ ), and for other variables the dependence on  $t$  is implied. Spectra and cross spectra  
177 are normalized to preserve variance; e.g.,  $\int S\{u\}df = \overline{u^2}$ , and  $\int C\{u,v\}df = \overline{uv}$ . The notations  
178  $S\{\mathbf{u}\} = (S\{u\}, S\{v\}, S\{w\})$ , and  $C\{\mathbf{u}\} = (C\{u,v\}, C\{u,w\}, C\{v,w\})$  denote the set of spectra and  
179 cross spectra for each velocity component and pairs of components, respectively.

180 Turbulence dissipation rates are computed as:

$$\epsilon = \frac{1}{\bar{U}} \left( \alpha \left\langle (S\{u\} + S\{v\} + S\{w\}) f^{5/3} \right\rangle_{f_{IS}} \right)^{3/2} \quad (1)$$

181 where  $\alpha = 0.5$  and  $\langle \rangle_{f_{IS}}$  denotes an average over the inertial subrange of the velocity spectra and  
182 where the signal-to-noise ratio is small (Lumley and Terray 1983; Sreenivasan 1995). Throughout  
183 this work, we take this average from 0.3 to 1 Hz for the  $u$  and  $v$  components, and 0.3 to 3 Hz for  
184 the  $w$  component.

### 185 3. Methodology

186 This work describes a method for correcting velocity measurements from a moving velocity  
187 sensor,  $\tilde{\mathbf{u}}_m$ , using independent measurements of that sensor's motion,  $\tilde{\mathbf{u}}_h$ , to remove the motion  
188 from the velocity measurements, and thus estimate the ‘motion corrected velocity’:

$$\tilde{\mathbf{u}}(t) = \tilde{\mathbf{u}}_m(t) + \tilde{\mathbf{u}}_h(t) \quad . \quad (2)$$

Note here that the ‘+’-sign is correct because head motion,  $\tilde{\mathbf{u}}_h$ , induces a measured velocity in the opposite direction of the head motion itself ( $\tilde{\mathbf{u}}_m = \tilde{\mathbf{u}} - \tilde{\mathbf{u}}_h$ ). This approach has been used to successfully correct sonic anemometer measurements of atmospheric turbulence (e.g., Edson et al. 1998; Miller et al. 2008). In the ocean, previous works have utilized inertial motion sensors to quantify the motion of multiscale profilers for the purpose of measuring the full spectrum of oceanic shear (Winkel et al. 1996), and to quantify the motion of thermistor sensors (Moum and Nash 2009), but the Edson et al. (1998) approach has not been documented for moored ADV measurements.

The Microstrain IMU available in the Nortek Vector ADV measures the linear acceleration,  $\mathbf{a}$ , rotational motion,  $\boldsymbol{\omega}$ , and orientation matrix,  $\mathbf{R}$ , of the ADV pressure case in the Earth reference frame at every time step of the ADV’s sampling. The motion of the ADV head is calculated from these signals as the sum of rotational and translational motion:

$$\begin{aligned}
 \tilde{\mathbf{u}}_h &= \tilde{\mathbf{u}}_\omega + \tilde{\mathbf{u}}_{\mathbf{a}} + \tilde{\mathbf{u}}_{\text{low}} \\
 &= \mathbf{R}^T \cdot \boldsymbol{\omega}^*(t) \times \ell^* + \int \langle \mathbf{a}(t) \rangle_{f_a} dt + \tilde{\mathbf{u}}_{\text{low}}
 \end{aligned} \tag{3}$$

Here, \* superscripts denote quantities in the ADV’s local coordinate system, and  $\ell^*$  is the vector from the IMU to the ADV head.  $\mathbf{R}^T$ —the inverse of the orientation matrix—rotates vectors from the ADV to the Earth reference frame. The notation  $\langle \cdot \rangle_{f_a}$  indicates a high-pass filtering operation at frequency  $f_a$ . The high-pass filter reduces low-frequency noise in  $\mathbf{a}$ —sometimes referred to as bias drift—that is amplified by integration (Barshan and Durrant-Whyte 1995; Bevly 2004; Gulmammadov 2009).  $\tilde{\mathbf{u}}_{\text{low}}$  is the low-frequency translational motion that is unresolved by  $\tilde{\mathbf{u}}_{\mathbf{a}}$ , and it is discussed in more detail below. To avoid double counting,  $\tilde{\mathbf{u}}_{\text{low}}$  should be estimated by applying the complementary low-pass filter (i.e., at  $f_a$ ) to the independent measurement of low-frequency motion. We use fourth order, zero-phase (bidirectional), Hanning filters for all filtering operations.

211 The noise levels of the IMU,  $\mathbf{n}_\omega$  and  $\mathbf{n}_a$ , are computed from ADV-IMU data collected while the  
212 instrument was resting motionless on a table for several hours. Where, for this motionless dataset,  
213 the noise levels are defined according to (3) with  $\mathbf{n}_\omega$  in place of  $\tilde{\mathbf{u}}_\omega$ , and  $\mathbf{n}_a$  in place of  $\tilde{\mathbf{u}}_a$ .

214 For quantifying  $\mathbf{n}_\omega$  we assume that  $|\ell^*| = 1$ , which is the approximate length of the ADV head  
215 cable.  $S\{\mathbf{n}_\omega\}$  is equal in all three components, because the rotation-rate sensor noise-levels are  
216 independent of orientation (Figure 6, yellow).  $S\{\mathbf{n}_\omega\}$  is several orders of magnitude lower than  
217 the velocity spectra we measured (grey region), and also more than an order of magnitude smaller  
218 than the Doppler noise levels of the ADV. This indicates that the precision of  $\tilde{\mathbf{u}}_\omega$  (i.e. the angular  
219 rate sensor) is adequate for making corrections to ADV velocity measurements.

220 The noise level of  $S\{\tilde{\mathbf{u}}_a\}$  (Figure 6, black), on the other hand, is dominated by a  $f^{-2}$  slope  
221 that results from integrating the low-frequency noise in  $\mathbf{a}$ . The horizontal ( $u$  and  $v$ ) spectra of  
222 these noise levels are identical, and so we only present one of them for simplicity (solid lines).  
223 The vertical spectra noise levels are different because the signal-to-noise ratio is larger (dashed  
224 black lines). High-pass filtering reduces the low-frequency noise (blue and red) so that it does  
225 not contaminate motion correction, but any real motion that does exist at these frequencies is lost  
226 (Egeland 2014; VanZwieten et al. 2015). This means there is a residual low-frequency translational  
227 motion,  $\tilde{\mathbf{u}}_{low}$ , that needs to be measured independently—or at the very least considered—when  
228 using ADV-IMU data from moving platforms.

229 For the SMB, the ADP bottom-track measured  $\tilde{\mathbf{u}}_{low}$ , and this measurement agrees with  $\tilde{\mathbf{u}}_a$  over  
230 a narrow frequency band (see Part I, appendix A), indicating that the ADP and IMU are resolving  
231 the same motion. When this is the case, it is trivial to select a frequency in the middle of the  
232 spectral overlap (in this case, we choose  $f_a = 0.2$  Hz), and high-pass and low-pass filter  $\tilde{\mathbf{u}}_a$  and  
233  $\tilde{\mathbf{u}}_{low}$ , respectively, then sum to estimate total translational motion.

234 The position of the TTM ADV can be estimated, relative to its base, by assuming the mooring  
235 acts like a rigid pole and using the IMU orientation matrix to estimate the pole’s ‘lean’. The posi-  
236 tion obtained from this model can then be differentiated to estimate  $\tilde{\mathbf{u}}_{\text{low}}$  (this model does not apply  
237 at high frequencies). Spectra of  $\tilde{\mathbf{u}}_{\text{low}}$  estimated using this approach for the June 2014 TTM deploy-  
238 ment (Figure 6, green) are plotted up to the point where they cross their respective  $S\{\tilde{\mathbf{u}}_{\mathbf{a}}\}$  noise  
239 level (black). Together, these two lines provide an ‘aggregate noise level’ of translational velocity  
240 estimates for the TTM: the rigid pole estimate of  $\tilde{\mathbf{u}}_{\text{low}}$  indicates the amplitude of unresolved mo-  
241 tion at low- $f$  (green), and  $S\{\tilde{\mathbf{u}}_{\mathbf{a}}\}$  indicates the limits of the IMU at high- $f$  (black). Coincidentally,  
242  $S\{\langle \rangle \tilde{\mathbf{u}}_{\mathbf{a}} \langle 0.03 \text{Hz} \rangle\}$  is not a terrible approximation for this aggregate noise level. Furthermore, because  
243 this aggregate noise level is at least a factor of 4 smaller than the velocity spectra we measured  
244 (shaded region), the results of motion correction are essentially identical whether we use the rigid  
245 pole model to estimate  $\tilde{\mathbf{u}}_{\text{low}}$ , or if we simply assume that  $\tilde{\mathbf{u}}_{\text{low}} = 0$ .

246 The choice of  $f_a$  does influence the effectiveness of motion correction (Figure 7). When  $f_a$  is  
247 too high (e.g., 0.3 Hz, red), the high-pass filter removes resolved motion from  $\tilde{\mathbf{u}}_h$  that could be  
248 used to correct velocity measurements. In particular, notice that the amplitude of the 0.15 Hz  
249 peak—which is clearly the result of motion contamination (grey line)—is reduced significantly  
250 when we preserve more  $\tilde{\mathbf{u}}_h$  information by reducing the high pass filter frequency to  $f_a = 0.03$  Hz.  
251 Further reducing  $f_a$  to 0.003 Hz does not reduce the peak further, but does increase the amplitude  
252 of the spectra at low-frequency. This increase is the IMU-accelerometer’s low-frequency bias drift  
253 (Figure 6) contaminating the velocity measurements. Therefore, we conclude that  $f_a = 0.03$  Hz is  
254 a convenient ‘middle’ frequency that reduces accelerometer bias-drift without destroying resolved  
255 motion of the TTM. The same  $f_a = 0.03$  Hz filter was selected, based on a similar analysis, for the  
256 turbulence torpedo.

257 Thus, we find that filter selection involves a trade-off between filtering out the bias drift noise  
258 at low-frequencies while not filtering out measured motion at high frequencies. In general, this  
259 will depend on the dynamics of the platform used to support the ADV, and the intensity of the  
260 turbulence being measured. When an independent measurement of  $\tilde{\mathbf{u}}_{\text{low}}$  is available the cross-  
261 coherence with  $\tilde{\mathbf{u}}_a$  can indicate a region of spectral overlap, and  $f_a$  can be selected at the midpoint.  
262 Lacking a reliable estimate of  $\tilde{\mathbf{u}}_{\text{low}}$ , the value of  $f_a$  that produces the lowest tke estimates is likely  
263 the best.

264 Additional details on motion correction—including a detailed accounting of the distinct co-  
265 ordinate systems of the IMU, ADV pressure case, and ADV head—can be found in Kilcher  
266 et al. (2016). Open-source Python tools for performing motion correction of ADV-IMU data—  
267 including scripts that write processed data in Matlab and tabulated formats—are available at  
268 <http://lkilcher.github.io/dolfin/>.

## 269 4. Results

### 270 a. Mean velocity

271 Figure 8 shows a comparison of  $\bar{\mathbf{u}}$  measured by an ADV-IMU mounted on the TTM, to an  
272 upward-looking ADP on the anchor. The profiler measurements—taken at the same depth as  
273 the ADV on the TTM—were contaminated by acoustic reflection from the strongback fin when  
274 it was inline with one of the profiler’s beams (see section 3). When those points (not shown  
275 in the figure) are excluded, this comparison shows excellent agreement between the ADV and  
276 ADP measurements of mean velocity. The  $\bar{u}$ ,  $\bar{v}$ , and  $\bar{w}$  components have a root-mean-square error  
277 of 0.05, 0.13, and  $0.03 \text{ ms}^{-1}$ , respectively. Although it is important to note that there is some  
278 discrepancy between ADP- and ADV-measured velocities (especially in  $\bar{v}$ , which is most likely

279 due to incomplete motion correction), the agreement between the magnitude and direction of these  
280 independent velocity measurements indicates that moored ADV-IMUs provide a reliable estimate  
281 of mean velocity in the Earth's reference frame.

282 *b. TTM spectra*

283 As discussed in detail in Part 1, the mooring motion of the TTM,  $S\{\mathbf{u}_h\}$ , has a peak at 0.1 to 0.2  
284 Hz from swaying of the mooring that is most likely driven by eddy shedding from the spherical  
285 buoy (Figure 9, red lines). There is also higher-frequency broadband motion that is associated with  
286 fluttering of the strongback fin around the mooring line. These motions are especially energetic  
287 in  $S\{v\}$  because this is the direction in which the TTM is most unstable. As is expected from  
288 fluid-structure interaction theory, the amplitude of these motions increases with increasing mean  
289 velocity (Morison et al. 1950).

290 The mooring motion contaminates the uncorrected ADV measurements of velocity,  $S\{\mathbf{u}_m\}$ ,  
291 whenever the amplitude of the motion is similar to or greater than the amplitude of the turbulence.  
292 Fortunately, much of this motion can be removed as detailed in Section 3. At high frequencies  
293 ( $f > 0.3$  Hz) for each mean-flow speed  $S\{\mathbf{u}\}$  are consistent with Kolmogorov's (1941) theory of  
294 isotropic turbulence: the spectra decay with a  $f^{-5/3}$  slope and have equal amplitude across the ve-  
295 locity components. At lower frequencies, the spectral 'roll-off' shape is similar to that measured  
296 by several others (e.g., Thomson et al. 2012; McMillan et al. 2016). The degree of agreement  
297 between Kaimal et al.'s (1972) semi-empirical form (cyan) and  $S\{\mathbf{u}\}$  is similar to that of Walter  
298 et al. (2011). This suggests that bottom-boundary layer physics are contributing to the turbulence  
299 at this site and depth.

300 For  $|\mathbf{u}| > 1.0 \text{ ms}^{-1}$ , motion correction improves  $S\{u\}$  and  $S\{v\}$  at frequencies as high as 3  
301 Hz. This indicates that tight synchronization between the ADV and IMU is important and that  
302 implementing asynchronous approaches to motion correction may be challenging.

303 As successful as motion correction is, some motion contamination is ‘persistent’. This is most  
304 notable in  $S\{v\}$  at the highest flow speeds ( $> 2.0 \text{ ms}^{-1}$ ): a peak at 0.15 Hz is an order of magnitude  
305 larger than a smooth spectral shape would suggest. This persistent motion contamination is evident  
306 to a lesser degree in  $S\{u\}$  for  $|\mathbf{u}| > 2 \text{ ms}^{-1}$ , and in  $S\{v\}$  at lower flow speeds.  $S\{w\}$  appears to  
307 have no persistent motion contamination because the amplitude of the motion in this direction is  
308 much lower than the measured spectra.

309 The amplitude of the persistent motion contamination peaks in  $S\{v\}$  at 0.15 Hz is a factor of 5 to  
310 10 times smaller than the amplitude of the ADV head motion itself. This observation suggests that  
311 the Microstrain IMU can be used to effectively correct mooring motion at this frequency when the  
312 amplitude of that motion is less than 5 times the amplitude of the real turbulence spectrum. As a  
313 result, we have chosen a value of 3 as a conservative estimate of motion correction’s effectiveness.

314 In addition to the primary benefit of correcting for mooring motion, the IMU measurements  
315 can also be used to identify and screen out persistent motion contamination. For example, one  
316 of the most common uses of turbulence spectra is for the calculation of  $\varepsilon$  and tke. For these  
317 purposes, and based on the relative amplitudes of the 0.15-Hz peaks, we assume that persistent  
318 motion contamination is likely where  $S\{\mathbf{u}_h\}/S\{\mathbf{u}\} > 3$ , and thereby exclude these regions from  
319 spectral fits.

320 In the present case, for  $u$ - and  $w$ -component spectra, this criteria only excludes a narrow range  
321 of frequencies around the 0.15-Hz motion peak for the largest flow speeds. This criteria is more  
322 restrictive of  $v$ -component spectra at high frequencies for  $\bar{U} > 1.0 \text{ ms}^{-1}$ , but this may be acceptable

323 because the amplitude of  $S\{v\}$  at these frequencies—i.e., in the isotropic inertial subrange—should  
324 be equal to that of  $S\{u\}$  and  $S\{w\}$  (Kolmogorov 1941).

325 Agreement of  $S\{v\}$  with that of  $S\{u\}$  and  $S\{w\}$  at frequencies  $> 0.3$  Hz indicates that motion  
326 correction is effective at those frequencies even when  $S\{\mathbf{u}_h\}/S\{\mathbf{u}\} \gtrsim 3$ . This outcome suggests  
327 that our screening threshold is excessively conservative at those frequencies, and that a more pre-  
328 cise screening threshold may be frequency dependent. For example, it might take into account the  
329  $f^{-2}$  character of the noise in  $S\{\mathbf{u}_a\}$  (Figure 6). For the purpose of this work, the  $S\{\mathbf{u}_h\}/S\{\mathbf{u}\} < 3$   
330 threshold for spectral fits is sufficient, and detailed characterization of the IMU’s motion- and  
331 frequency-dependent noise level is left for future work.

332 *c. StableMoor Spectra*

333 Spectra of SMB motion have broader peaks, with a maximum amplitude that is approximately  
334 half the frequency of the TTM spectral peak (0.06 Hz, Figure 10). The motion of this platform also  
335 does not have high-frequency “subpeaks” or other high-frequency broadband excitation (Part 1).  
336 These characteristics are due to the more massive and hydrodynamically streamlined properties of  
337 the SMB compared to the TTM.

338 Like the TTM, the motion-corrected spectra from the SMB are consistent with turbulence theory  
339 and previous observations. A notable distinction from the TTM, however, is that there are no  
340 obvious persistent motion contamination peaks. That is, this measurement system provides an  
341 accurate estimate of the turbulence spectra at this location from low frequencies to more than 1  
342 Hz—well into the inertial subrange—for all three components of velocity.

343 Note that this level of accuracy cannot be obtained without the independent estimate of  $\mathbf{u}_{low}$   
344 (from the bottom-tracking ADP). If we assume that  $\mathbf{u}_{low} = 0$ , a similar plot to Figure 10 (not  
345 shown) reveals persistent motion-contamination peaks and troughs in  $S\{u\}$  and  $S\{v\}$  regardless

346 of the choice of  $f_a$ . This indicates that the low-frequency translational motion of the SMB that  
347 is important to motion correction is poorly resolved by the IMU's accelerometer. In other words,  
348 compared to the TTM, the SMB provides a more accurate measurement of turbulence when it  
349 includes an independent measure of  $\mathbf{u}_{\text{low}}$ , but it does no better—and perhaps worse—when it does  
350 not.

351 *d. Torpedo spectra*

352  $S\{u_h\}$  and  $S\{v_h\}$  for the turbulence torpedo is broadband and  $S\{w_h\}$  motion has a narrow peak  
353 at 0.3 Hz (Figure 11). Because  $\mathbf{u}_h$  is estimated using  $f_a = 0.03$  Hz and assuming  $\mathbf{u}_{\text{low}} = 0$ , its  
354 spectra rolls off quickly below  $f_a$ . Motion correction of the torpedo data appears to effectively  
355 remove a motion peak from  $S\{w\}$  at 0.3 Hz, and corrects  $S\{v\}$  between 0.04 and 0.6 Hz.  $S\{u\}$   
356 is mostly unaffected by motion at these frequencies, because the torpedo motion is smaller than  
357 the turbulence in this direction. At frequencies below  $f_a$ ,  $S\{u\}$  and  $S\{v\}$  increase dramatically.  
358 This suggests that unresolved, low-frequency motion of the torpedo is contaminating the velocity  
359 measurements at these frequencies. It may be possible to correct for some of this contamination  
360 using a measurement of the ship's motion as a proxy for the torpedo's low-frequency motion,  
361 but this has not been done. Still, above  $f_a$ , the torpedo appears to provide a reliable estimate of  
362 spectral amplitude in the inertial subrange and can therefore be used to estimate  $\varepsilon$ . Considering  
363 the simplicity of the platform, it may be a useful option for quantifying this turbulence statistic in  
364 a variety of scenarios. If a GPS is positioned above it, it may be capable of providing even more.

365 *e. Cross Spectra*

366 Cross-spectra indicate the correlation between different velocity components as a function of fre-  
367 quency, and their integrals are the Reynold's stresses. Head motion cross-spectra,  $C\{\mathbf{u}_h\}$  (Figure

12, red), and uncorrected velocity cross-spectra,  $C\{\mathbf{u}_m\}$  (black), from TTM measurements have  
large peaks at the same frequency (0.15 Hz) as peaks in auto-spectra (Figure 9). This indicates  
that mooring motion contaminates the uncorrected cross-spectral velocity measurements, and that  
Reynold's stress estimates based on uncorrected velocity measurements will be contaminated by  
mooring motion.

Fortunately, motion corrected velocity cross-spectra,  $C\{\mathbf{u}\}$  (Figure 12, blue), have reduced  
cross-spectral amplitudes at these frequencies. This indicates that motion correction reduces motion  
contamination to produce more reliable estimates of velocity cross spectra and Reynold's  
stresses (Figure 12). Notably, the low standard deviation of  $fC\{\mathbf{u}\}$  (indicated by the blue shading)  
compared to the mean values of  $fC\{\mathbf{u}_h\}$  and  $fC\{\mathbf{u}_m\}$ —at the frequencies of maximum motion—  
indicates that even the individual values of  $C\{\mathbf{u}\}$  are reduced at these frequencies, compared to  
 $C\{\mathbf{u}_m\}$ , not just their mean.

These results indicate that motion-corrected TTM velocity measurements can be used to estimate  
turbulence Reynold's stresses. Without motion correction, Reynold's stress estimates would be  
contaminated by the large peaks in the cross spectra that are caused by the swaying and fluttering  
motion of the TTM vane. Cross-spectra of TTM data for other velocity ranges (i.e.,  $< 2 \text{ ms}^{-1}$ ),  
and cross-spectra from the SMB show similar results (not shown). However, we note that because  
the SMB is less-stable in pitch than the TTM (see Part I for details), the TTM provides a more  
accurate estimates of  $\bar{uw}$ .

In order to compare the cross-spectra to other measurements, we normalize them following  
Kaimal et al. (1972) as:  $\hat{C}\{u, w\}(\hat{f}) = -C\{u, w\}f_o/u_*^2$ , where  $f_o = \bar{U}/z$  and  $\hat{f} = f/f_o$ . When  
plotted on a log-log scale,  $\hat{C}\{u, w\}$  has a  $\hat{f}^{-7/3}$  high-frequency spectral slope that is consistent  
with other measurements (Figure 13). At low-frequency, the cross-spectra are more than 10x  
smaller than the semi-empirical Kaimal form, but this discrepancy is consistent with other mea-

surements of cross-spectra. In particular, Walter et al. (2011) observed a half-decade reduction from the Kaimal form near the seafloor, and measurements from an ADV positioned 4.6 m above the seafloor on a fixed tripod at a different site in Puget Sound show a similar degree of deviation as observed here (Thomson et al. 2012).

While one might be inclined to attribute the discrepancy between these estimates and the Kaimal form to normalization by local  $u_*$ , the agreement between auto-spectra and their Kaimal form suggests otherwise (Figure 9). Instead, we conclude that either the Kaimal cross-spectra do not apply universally at distances far from the bottom boundary, or the spectra are being modified by physics other than bottom boundary layer driven turbulence. Either way, the agreement of TTM-measured cross-spectra with measurements from stationary platforms is interpreted as an indication that this platform can resolve cross-spectra and Reynold's stresses.

## 5. Discussion

Ideally, moored motion-corrected turbulence velocity measurements would be validated against simultaneous independent validated measurements of turbulence velocity at the same scales, time, and location. Accomplishing this, however, involves significant technical challenges that are not easily overcome—most notably the difficulty of measuring turbulence at the same point as the moving ADV. A slightly less ideal but much more realistic confirmation of the methodology might involve comparing the statistics of moored turbulence measurements to those from a nearby fixed platform, or a fixed platform placed at the same location at a different time (e.g., the “tripod” platform described in Thomson et al. 2012). Unfortunately, to our knowledge, these measurements have not yet been made.

The previous section showed that the shape of the turbulence velocity spectra from moored ADVs is consistent with Kolmogorov's theory of locally isotropic turbulence, which has been ob-

415 served consistently in turbulence measurements for decades (Kolmogorov 1941; Grant et al. 1962;  
 416 McMillan et al. 2016). This is interpreted as the first indication that the measurement systems  
 417 presented are capable of accurately resolving turbulence. The degree to which uncorrected spec-  
 418 tra were corrected toward this theoretical and observationally confirmed shape is interpreted as a  
 419 measure of the improvement of the spectral estimates by motion correction. This section takes  
 420 that reasoning one step further to demonstrate that motion-corrected velocity measurements can  
 421 produce estimates of turbulence statistics that are consistent with the physical processes that can  
 422 be reasonably assumed to dominate the measurement site.

423 Figure 14 presents a time series of the mean velocity (A) and several turbulence statistics that  
 424 were measured during the June 2014 TTM deployment. This figure shows the evolution of the flow  
 425 through Admiralty Inlet during 1.5 tidal cycles. The tke (B), Reynold's stresses (C), dissipation,  
 426 and one component of turbulence production (D) grow and strengthen with ebb or flood then  
 427 subside during slack tide. This component of turbulence production is:

$$P_{uz} = \bar{uw} \frac{\partial \bar{u}}{\partial z} . \quad (4)$$

428 Where  $\partial \bar{u} / \partial z$  is computed from the two ADVs on the TTM. The highest values of  $\varepsilon$  and  $P_{uz}$  occur  
 429 at the peak of the ebb or flood, which is in agreement with other measurements in tidal channels.  
 430 The agreement of the magnitude of  $P_{uz}$  with  $\varepsilon$  at those times suggests a local production-dissipation  
 431 balance that is often observed in tidally forced channels (Trowbridge et al. 1999; Stacey et al.  
 432 1999b; McMillan et al. 2016). At other times, the value of  $P_{uz}$  is insufficient to balance  $\varepsilon$  or is  
 433 negative.

434 Inspection of the negative  $P_{uz}$  values reveals that most of them are caused by a reversed sign of  $\bar{uw}$   
 435 rather than a reversed sign of  $\partial u / \partial z$  (i.e., when compared to the sign of  $u$ ). This finding suggests  
 436 that uncertainty in  $\bar{uw}$  may be contributing to discrepancies between  $P_{uz}$  and  $\varepsilon$ . Furthermore,

437 considering the complex nature of the bathymetry and shoreline at this site (i.e., the headland), it  
438 is not surprising that  $P_{uz}$  does not perfectly balance  $\varepsilon$ . Other terms of the tke equation are likely  
439 to be important, such as turbulence advection, other components of production, and turbulent  
440 transport. The fact that  $P_{uz}$  and  $\varepsilon$  are in near balance as often as they are indicates that bottom  
441 boundary layer physics are important to the turbulence dynamics at this site.

442 Given the assumptions implicit in this comparison and the discussion above, agreement between  
443  $P_{uz}$  and  $\varepsilon$ —especially for the highest values of  $\varepsilon$ —suggests the turbulent boundary layer reaches  
444 the depth of these measurements (10 m) during the highest flow speeds (Figure 15). This result  
445 is further supported by a comparison of  $\bar{U}$  with  $\varepsilon$  (Figure 16). Here we see a  $\varepsilon \propto \bar{U}^3$  dependence  
446 that is again suggestive of bottom boundary layer physics (Trowbridge 1992; Nash et al. 2009). At  
447 lower flow speeds,  $\varepsilon$  deviates from this relationship, which suggests that the boundary layer is no  
448 longer the dominant physical process at the depth of these measurements.

449 There are two intriguing differences between the ebb and flood datasets: 1) the drag coefficient  
450 relating  $\varepsilon$  to  $\bar{U}^3$  is larger for ebbs, and 2) the fit does not hold as well for low flow speeds (Figure  
451 16). These details are not surprising considering the complex bathymetry at the test site (Figure  
452 1). In particular, the flow immediately upstream of the measurement site is exposed to much  
453 more bathymetric curvature—i.e. from the headland—during ebb (when  $\bar{u}$  is  $> 0$ ) than the during  
454 flood ( $\bar{u} < 0$ ). Based on this, one might expect flow separation (turbulence advection), turbulence  
455 production, or turbulence transport emanating from the headland to have a stronger impact on  
456 the flow at this site during ebb than flood. These effects are a likely contributor to the distinct  
457 relationships observed in Figure 16.

458 The hypothesis that the headland is a key contributor to the turbulence dynamics at this site  
459 suggests that terms such as cross-stream turbulence advection,  $\bar{v}\partial\text{tke}/\partial y$ , the lateral turbulent  
460 transport terms,  $\partial\bar{u}_i\bar{u}_i\bar{v}/\partial y$ , or lateral shear production,  $\bar{u}\bar{v}\partial\bar{u}/\partial y$ , may contribute significantly to

the dynamics of turbulence at this site. While we did not measure stratification profiles during these measurements, we do not typically expect buoyancy flux to play a dominant role due to the fact that this region tends to be tidally well-mixed (Geyer and Cannon 1982). In summary, bottom boundary layer physics seems to be the dominant process at the measurement site, with lateral advection, lateral transport, and lateral production of tke also potentially contributing—especially during ebb. A more detailed analysis of the turbulence and momentum dynamics of this headland is left for future work (e.g., similar to Warner et al. 2013).

## 6. Conclusion

This work presents a methodology for measuring turbulence from moored ADV-IMUs and demonstrates that motion correction reduces mooring motion-contamination. Comparison of spectra of ADV head motion,  $S\{\mathbf{u}_h\}$ , to that of motion-corrected,  $S\{\mathbf{u}\}$ , and uncorrected spectra,  $S\{\mathbf{u}_m\}$ , reveals that motion correction improves spectral estimates of moored ADV measurements. In particular, we found that motion-corrected spectra have spectral shapes that are similar to previous measurements of tidal-channel turbulence and have  $f^{-5/3}$  spectral slopes at high frequencies. This finding suggests that the motion-corrected spectra resolve the inertial subrange predicted by Kolmogorov’s theory of locally isotropic turbulence.

Motion correction reduces motion contamination for all platforms we presented but it does not necessarily remove it completely. This outcome seems to depend on the relative amplitude of platform motion compared to the underlying turbulence being measured. The most notable example of this is from TTM  $S\{v\}$ , which have large-amplitude “swaying” peaks at 0.15 Hz that interrupts the frequently observed ‘roll-off’ between the low-frequency ‘energy containing scales’ and the  $f^{-5/3}$  inertial subrange.

483 The possibility of persistent motion contamination requires that turbulence measurements from  
484 moored, motion-corrected ADV-IMUs be interpreted with care. An inspection of spectra presented  
485 here suggests that excluding spectral regions where  $S\{\mathbf{u}_h\}/S\{\mathbf{u}\} > 3$  removes persistent-motion  
486 contamination peaks while still preserving spectral regions where motion correction is effective.  
487 Using this criteria, it is then possible to produce spectral fits that exclude persistent-motion con-  
488 tamination, and provide reliable estimates of turbulence quantities of interest (e.g.,  $\varepsilon$  and tke).

489 We have also shown that motion correction reduces motion contamination in cross spectra. This  
490 finding is important because it suggests that moored ADV-IMU measurements may be used to  
491 produce reliable estimates of Reynolds stresses. We utilized these stress estimates and vertical  
492 shear estimates, both from the TTM, to estimate  $P_{uz}$ .

493 Finally, we have shown that  $\varepsilon$  estimates based on motion-corrected spectra scale with  $\bar{U}^3$ , and  
494 balance  $P_{uz}$  estimates during peak ebb and flood. Together, these results indicate that bottom  
495 boundary layer physics are a dominant process at this site, and that the boundary layer reaches the  
496 height of the ADV-IMUs (10 m) during ebb and flood. The degree of agreement between  $P_{uz}$  and  $\varepsilon$   
497 also serves as an indicator of the self-consistency of moored ADV-IMU turbulence measurements.

498 *Acknowledgments.* Many thanks to Joe Talbert, Alex DeKlerk, Captain Andy Reay-Ellers, Jen-  
499 nifer Rinker, Maricarmen Guerra, and Eric Nelson in assisting with data collection. The authors  
500 are also grateful to James VanZwieten, Matthew Egeland and Marshall Richmond for discussion  
501 on the details of this work.

502 Thanks to the open-source software community for the tools used in this work, especially the  
503 developers of LATEX, Python, NumPy, Matplotlib, git, and GNU emacs.

504 This work was supported by the U.S. Department of Energy under Contract No. DE-AC36-  
505 08GO28308 with the National Renewable Energy Laboratory. Funding for the work was provided

506 by the DOE Office of Energy Efficiency and Renewable Energy, Wind and Water Power Technolo-  
507 gies Office.

508 The U.S. Government retains and the publisher, by accepting the article for publication, ac-  
509 knowledges that the U.S. Government retains a nonexclusive, paid-up, irrevocable, worldwide  
510 license to publish or reproduce the published form of this work, or allow others to do so, for U.S.  
511 Government purposes.

512    **References**

- 513    Afgan, I., J. McNaughton, S. Rolfo, D. Apsley, T. Stallard, and P. Stansby, 2013: Turbulent flow  
514    and loading on a tidal stream turbine by les and rans. *International Journal of Heat and Fluid*  
515    *Flow*, **43**, 96–108.
- 516    Alexander, S. R., and P. E. Hamlington, 2015: Analysis of turbulent bending moments in tidal  
517    current boundary layers. *Journal of Renewable and Sustainable Energy*, **7 (6)**, 063 118.
- 518    Alford, M. H., 2010: Sustained, full-water-column observations of internal waves and mixing near  
519    mendocino escarpment. *Journal of Physical Oceanography*, **40 (12)**, 2643–2660, doi:10.1175/  
520    2010JPO4502.1.
- 521    Axford, D., 1968: On the accuracy of wind measurements using an inertial platform in an aircraft,  
522    and an example of a measurement of the vertical mesostructure of the atmosphere. *Journal of*  
523    *Applied Meteorology*, **7 (4)**, 645–666.
- 524    Barshan, B., and H. F. Durrant-Whyte, 1995: Inertial navigation systems for mobile robots. *IEEE*  
525    *Transactions on Robotics and Automation*, **11 (3)**, 328–342.
- 526    Bevly, D. M., 2004: Global positioning system (gps): A low-cost velocity sensor for correcting in-  
527    erial sensor errors on ground vehicles. *Journal of dynamic systems, measurement, and control*,  
528    **126 (2)**, 255–264.
- 529    Cartwright, G. M., C. T. Friedrichs, P. J. Dickhudt, T. Gass, and F. H. Farmer, 2009: Using the  
530    acoustic doppler velocimeter (adv) in the mudbed real-time observing system. *Marine Technol-  
531    ogy for Our Future: Global and Local Challenges*.
- 532    Doherty, K., D. Frye, S. Liberatore, and J. Toole, 1999: A moored profiling instrument\*. *Journal*  
533    *of Atmospheric and Oceanic Technology*, **16 (11)**, 1816–1829.

- 534 Edson, J. B., A. A. Hinton, K. E. Prada, J. E. Hare, and C. W. Fairall, 1998: Direct covariance  
535 flux estimates from mobile platforms at sea\*. *Journal of Atmospheric and Oceanic Technology*,  
536 **15** (2), 547–562, doi:10.1175/1520-0426(1998)015<0547:DCFEFM>2.0.CO;2.
- 537 Egeland, M. N., 2014: Spectral evaluation of motion compensated ADV systems for ocean turbu-  
538 lence measurements. Ph.D. thesis, Florida Atlantic University.
- 539 Fer, I., and M. B. Paskyabi, 2014: Autonomous ocean turbulence measurements using shear probes  
540 on a moored instrument. *Journal of Atmospheric and Oceanic Technology*, **31** (2), 474–490, doi:  
541 10.1175/JTECH-D-13-00096.1.
- 542 Finlayson, D., 2005: Combined bathymetry and topography of the Puget Lowlands,  
543 Washington state. URL <https://www.ocean.washington.edu/data/pugetsound/psdem2005.html>,  
544 g1230485.zip, retrieved September 2014.
- 545 Geyer, R. W., M. E. Scully, and D. K. Ralston, 2008: Quantifying vertical mixing in estuaries.  
546 *Environmental Fluid Mechanics*, **8**, 495–509, doi:10.1007/s10652-008-9107-2.
- 547 Geyer, W. R., and G. A. Cannon, 1982: Sill processes related to deep water renewal in a fjord. *Jour-*  
548 *nal of Geophysical Research: Oceans*, **87** (C10), 7985–7996, doi:10.1029/JC087iC10p07985.
- 549 Goodman, L., E. R. Levine, and R. G. Lueck, 2006: On measuring the terms of the turbulent  
550 kinetic energy budget from an auv. *Journal of Atmospheric and Oceanic Technology*, **23** (7),  
551 977–990, doi:10.1175/JTECH1889.1.
- 552 Grant, H. L., R. W. Stewart, and A. Moilliet, 1962: Turbulence spectra from a tidal channel.  
553 *Journal of Fluid Mechanics*, **12**, 241–263.
- 554 Guerra Paris, M., and J. Thomson, 2017: Turbulence measurements from 5-beam acoustic doppler  
555 current profilers. *Journal of Atmospheric and Oceanic Technology*.

- 556 Gulmammadov, F., 2009: Analysis, modeling and compensation of bias drift in mems inertial  
557 sensors. *Recent Advances in Space Technologies, 2009. RAST'09. 4th International Conference*  
558 on, IEEE, 591–596.
- 559 Gunawan, B., V. S. Neary, and J. Colby, 2014: Tidal energy site resource assessment in the East  
560 River tidal strait, near Roosevelt Island, New York, NY (USA). *Renewable Energy*, **71**, 509–  
561 517, doi:10.1016/j.renene.2014.06.002.
- 562 Hand, M. M., N. D. Kelley, and M. J. Balas, 2003: Identification of wind turbine response to  
563 turbulent inflow structures. Tech. Rep. NREL/CP-500-33465, National Renewable Energy Lab-  
564 oratory.
- 565 Harding, S., L. Kilcher, and J. Thomson, 2017: Turbulence measurements from compliant moor-  
566 ings - part 1: Motion characterization, in review.
- 567 Kaimal, J. C., J. C. Wyngaard, Y. Izumi, and O. R. Cote, 1972: Spectral characteristics of surface-  
568 layer turbulence. *Quart. J. Roy. Meteor. Soc*, **98 (417)**, 563–689.
- 569 Kelley, N. D., B. J. Jonkman, G. N. Scott, J. T. Bialasiewicz, and L. S. Redmond, 2005: The impact  
570 of coherent turbulence on wind turbine aeroelastic response and its simulation. *WindPower*,  
571 Denver, Colorado, NREL/CP-500-38074, may 15-18.
- 572 Kilcher, L., J. Thomson, J. Talbert, and A. DeKlerk, 2016: Measuring turbulence from moored  
573 acoustic Doppler velocimeters: A manual to quantifying inflow at tidal energy sites. 9 62979,  
574 National Renewable Energy Laboratory. URL [www.nrel.gov/docs/fy16osti/62979.pdf](http://www.nrel.gov/docs/fy16osti/62979.pdf).
- 575 Kim, S. C., C. T. Friedrichs, J. P.-Y. Maa, and L. D. Wright, 2000: Estimating bottom stress in  
576 tidal boundary layer from acoustic doppler velocimeter data. *Journal of Hydraulic Engineering*,  
577 399–406.

- 578 Kolmogorov, A. N., 1941: Dissipation of energy in the locally isotropic turbulence. *Dokl. Akad.*  
579 *Nauk SSSR*, **32** (1), 16–18, URL <http://www.jstor.org/stable/51981>.
- 580 Kraus, N. C., A. Lohrmann, and R. Cabrera, 1994: A new acoustic meter for measuring 3D  
581 laboratory flows. *Journal of Hydraulic Engineering*, **120**, 406–412.
- 582 Lohrmann, A., R. Cabrera, G. Gelfenbaum, and J. Haines, 1995: Direct measurements of reynolds  
583 stress with an acoustic doppler velocimeter. *Current Measurement, 1995., Proceedings of the*  
584 *IEEE Fifth Working Conference on*, 205–210, doi:10.1109/CCM.1995.516175.
- 585 Lorke, A., 2007: Boundary mixing in the thermocline of a large lake. *Journal of Geophysical*  
586 *Research: Oceans*, **112** (C9), n/a–n/a, doi:10.1029/2006JC004008, c09019.
- 587 Lueck, R. G., and D. Huang, 1999: Dissipation measurement with a moored instrument in a swift  
588 tidal channel. *Journal of atmospheric and oceanic technology*, **16**, 1499–1505.
- 589 Lumley, J., and E. Terray, 1983: Kinematics of turbulence convected by a random wave field.  
590 *Journal of Physical Oceanography*, **13** (11), 2000–2007.
- 591 McCaffrey, K., B. Fox-Kemper, P. E. Hamlington, and J. Thomson, 2015: Characterization of  
592 turbulence anisotropy, coherence, and intermittency at a prospective tidal energy site: Observa-  
593 tional data analysis. *Renewable Energy*, **76**, 441–453.
- 594 McMillan, J. M., A. E. Hay, R. G. Lueck, and F. Wolk, 2016: Rates of dissipation of turbulent  
595 kinetic energy in a high reynolds number tidal channel. *Journal of Atmospheric and Oceanic*  
596 *Technology*, **33** (4), 817–837, doi:10.1175/JTECH-D-15-0167.1.
- 597 MicroStrain, I., 2010: Technical note: Coning and sculling. Tech. Rep. I0019, MicroStrain. URL  
598 [http://files.microstrain.com/TN-I0019\\_3DM-GX3-25\\_\\_Coning\\_And\\_Sculling.pdf](http://files.microstrain.com/TN-I0019_3DM-GX3-25__Coning_And_Sculling.pdf).

- 599 MicroStrain, I., 2012: *3DM-GX3-15,-25 MIP Data Communications Protocol*. URL <http://files.microstrain.com/3DM-GX3-15-25-MIP-Data-Communications-Protocol.pdf>, retrieved  
600 //files.microstrain.com/3DM-GX3-15-25-MIP-Data-Communications-Protocol.pdf, retrieved  
601 January 2014.
- 602 Miller, S. D., T. S. Hristov, J. B. Edson, and C. A. Friehe, 2008: Platform motion effects on  
603 measurements of turbulence and air-sea exchange over the open ocean. *Journal of Atmospheric*  
604 *and Oceanic Technology*, **25** (9), 1683–1694, doi:10.1175/2008JTECHO547.1.
- 605 Morison, J. R., J. W. Johnson, and S. A. Schaaf, 1950: The force exerted by surface waves on  
606 piles. *Journal of Petroleum Technology*, **2** (05), 149–154.
- 607 Moum, J., and J. Nash, 2009: Mixing measurements on an equatorial ocean mooring. *Journal of*  
608 *Atmospheric and Oceanic Technology*, **26** (2), 317–336.
- 609 Mücke, T., D. Kleinhans, and J. Peinke, 2011: Atmospheric turbulence and its influence on the  
610 alternating loads on wind turbines. *Wind Energy*, **14**, 301–316.
- 611 Nash, J. D., L. F. Kilcher, and J. N. Moum, 2009: Structure and composition of a strongly  
612 stratified, tidally pulsed river plume. *Journal of Geophysical Research*, **114**, C00B12, doi:  
613 10.1029/2008JC005036.
- 614 Nash, J. D., E. Kunze, J. M. Toole, and R. W. Schmitt, 2004: Internal tide reflection and turbulent  
615 mixing on the continental slope. *Journal of Physical Oceanography*, **34** (5), 1117–1134, doi:  
616 10.1175/1520-0485(2004)034<1117:ITRATM>2.0.CO;2.
- 617 Nortek, 2005: *Vector Current Meter User Manual*. Vangkroken 2, NO-1351 RUD, Norway, h ed.
- 618 Paskyabi, M. B., and I. Fer, 2013: Turbulence measurements in shallow water from a subsurface  
619 moored moving platform. *Energy Procedia*, **35**, 307 – 316, doi:10.1016/j.egypro.2013.07.183.

- 620 Perlin, A., and J. N. Moum, 2012: Comparison of thermal variance dissipation rates from moored  
621 and profiling instruments at the equator. *Journal of Atmospheric and Oceanic Technology*.
- 622 Polagye, B., and J. Thomson, 2013: Tidal energy resource characterization: methodology and field  
623 study in admiralty inlet, Puget Sound, WA (USA). *Proceedings of the Institution of Mechanical  
624 Engineers, Part A: Journal of Power and Energy*, **227** (3), 352–367.
- 625 Rippeth, T. P., E. Williams, and J. H. Simpson, 2002: Reynolds stress and turbulent en-  
626 ergy production in a tidal channel. *Journal of Physical Oceanography*, **32**, 1242–1251, doi:  
627 10.1175/1520-0485(2002)032\$1242:RSATEP\$2.0.CO;2.
- 628 Sreenivasan, K. R., 1995: On the universality of the Kolmogorov constant. *Physics of Fluids*, **7**,  
629 2778–2784.
- 630 Stacey, M. T., S. G. Monismith, and J. R. Burau, 1999a: Measurements of reynolds stress  
631 profiles in unstratified tidal flow. *J. Geophys. Res.*, **104** (C5), 10 933–10 949, doi:10.1029/  
632 1998JC900095.
- 633 Stacey, M. T., S. G. Monismith, and J. R. Burau, 1999b: Observations of turbulence in a partially  
634 stratified estuary. *Journal of Physical Oceanography*, **29**, 1950–1970.
- 635 Thomson, J., B. Polagye, V. Durgesh, and M. Richmond, 2012: Measurements of turbulence at  
636 two tidal energy sites in Puget Sound, WA. *Journal of Oceanic Engineering*, **37** (3), 363–374,  
637 doi:10.1109/JOE.2012.2191656.
- 638 Trowbridge, J. H., 1992: A simple description of the deepening and structure of a stably stratified  
639 flow driven by a surface stress. *Journal of Geophysical Research*, **97**, 15 529–15 543.

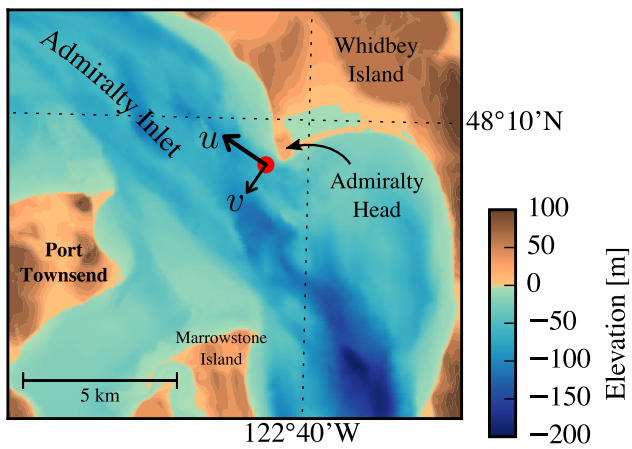
- 640 Trowbridge, J. H., W. R. Geyer, M. M. Bowen, and A. J. I. Williams, 1999: Near-bottom turbulence measurements in a partially mixed estuary: turbulent energy balance, velocity structure  
641 and along-channel momentum balance. *Journal of Physical Oceanography*, **29**, 3056–3072.
- 642
- 643 van der Walt, S., S. C. Colbert, and G. Varoquaux, 2011: The numpy array: A structure for efficient  
644 numerical computation. *Computing in Science & Engineering*, **13**, 22–30, doi:10.1109/MCSE.  
645 2011.37.
- 646 VanZwieten, J. H., M. N. Egeland, K. D. von Ellenrieder, J. W. Lovenbury, and L. Kilcher, 2015:  
647 Experimental evaluation of motion compensated adv measurements for in-stream hydrokinetic  
648 applications. *Current, Waves and Turbulence Measurement (CWTM), 2015 IEEE/OES Eleventh*,  
649 1–8, doi:10.1109/CWTM.2015.7098119.
- 650 Voulgaris, G., and J. H. Trowbridge, 1998: Evaluation of the acoustic doppler velocimeter (adv)  
651 for turbulence measurements. *Journal of Atmospheric and Oceanic technology*, **15**, 272–289.
- 652 Walter, R. K., N. J. Nidzieko, and S. G. Monismith, 2011: Similarity scaling of turbulence spectra  
653 and cospectra in a shallow tidal flow. *Journal of Geophysical Research: Oceans*, **116 (C10)**.
- 654 Warner, S. J., P. MacCready, J. N. Moum, and J. D. Nash, 2013: Measurement of tidal form drag  
655 using seafloor pressure sensors. *Journal of Physical Oceanography*, **43 (6)**, 1150–1172.
- 656 Wiles, P. J., T. P. Rippeth, J. H. Simpson, and P. J. Hendricks, 2006: A novel technique for  
657 measuring the rate of turbulent dissipation in the marine environment. *Geophysical Research  
658 Letters*, **33**, 21 608.
- 659 Winkel, D., M. Gregg, and T. Sanford, 1996: Resolving oceanic shear and velocity with the multi-  
660 scale profiler. *Journal of Atmospheric and Oceanic Technology*, **13 (5)**, 1046–1072.

- 661 Wyngaard, J. C., L. Rockwell, and C. A. Friehe, 1985: Errors in the measurement of turbulence  
662 upstream of an axisymmetric body. *Journal of Atmospheric and Oceanic Technology*, **2** (4),  
663 605–614.
- 664 Zhang, Y., K. Streitlien, J. G. Bellingham, and A. B. Baggeroer, 2001: Acoustic doppler ve-  
665 locimeter flow measurement from an autonomous underwater vehicle with applications to deep  
666 ocean convection. *Journal of Atmospheric and Oceanic Technology*, **18** (12), 2038–2051, doi:  
667 10.1175/1520-0426(2001)018<2038:ADVFMF>2.0.CO;2.

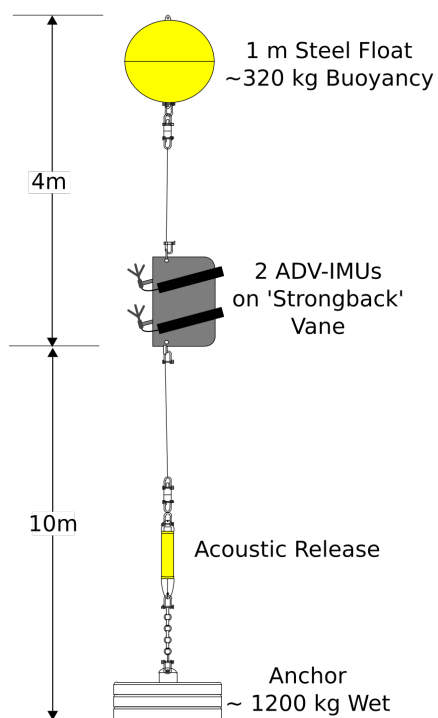
## 668 LIST OF FIGURES

669	<b>Fig. 1.</b>	Bathymetry of Admiralty Inlet near Port Townsend, Washington, U.S.A. (Finlayson 2005). The red dot indicates the location of all measurements. The positive $u$ direction is the direction of ebb flow (thick arrow originating from red dot), and positive $v$ is away from Admiralty Head (smaller arrow).	35
673	<b>Fig. 2.</b>	Schematic diagram of the TTM; not to scale. A pop-up buoy for anchor recovery is not shown, for simplicity.	36
675	<b>Fig. 3.</b>	TTM components on the deck of the R/V Jack Robertson. The TTM includes two ADVs, with pressure cases mounted on opposite sides of the fin. The anchor stack includes a pop-up buoy for retrieval. The green arrow indicates the vector from the IMU to the ADV head (face of the transmit transducer).	37
679	<b>Fig. 4.</b>	Top: Alex DeKlerk checks to ensure that the SMB buoy is properly fastened to its anchor; the RDI workhorse ADP can be seen in the rear instrument bay. A bridle is draped across the top of the buoy for deployment and recovery, and a small marker buoy fastened to the tail is useful during recovery. Bottom: a close-up of the SMB buoy with the ADV head and the top of its pressure case. The green arrow indicates the vector from the IMU to the ADV head.	38
685	<b>Fig. 5.</b>	The turbulence platform showing details of the ADV head and pressure case configuration. The green arrow indicates the vector from the IMU to the ADV head. The head cable was taped out of the way beneath the sounding weight tail fins shortly after taking this photo.	39
688	<b>Fig. 6.</b>	The spectral noise levels of rotational velocity ( $S\{\mathbf{n}_\omega\}$ , yellow) and translational velocity ( $S\{\mathbf{n}_a\}$ , black) estimated from an ADV-IMU resting motionless on a table. Solid and dashed lines indicate the horizontal and vertical components, respectively, of $S\{\mathbf{n}_a\}$ and $S\{\mathbf{u}_{low}\}$ . The $\mathbf{n}_a$ signals are unfiltered (black), and high-pass filtered at 0.03 Hz (blue) and 0.3 Hz (red); vertical dotted lines indicate the filter frequency. Green lines are an estimate of $\mathbf{u}_{low}$ for the TTM. Grey horizontal lines indicate the horizontal (solid) and vertical (dashed) ADV noise levels. The shaded region indicates the range of $S\{u\}$ presented in the next section.	40
695	<b>Fig. 7.</b>	Motion-corrected velocity spectra, $S\{\mathbf{u}\}$ , for a range of high-pass filter frequencies: $f_a = 0.3$ Hz (thin red), 0.03 Hz (blue), and 0.003 Hz (thick black). The vertical dotted lines indicate the filter frequency. The thick grey line is $S\{\mathbf{u}_h\}$ for $f_a = 0.003$ Hz. The data are from the June 2014 TTM deployment when $2.0 <  \bar{u}  < 2.5 \text{ ms}^{-1}$ .	41
699	<b>Fig. 8.</b>	Time series of tidal velocity in June 2012 at Admiralty Head from ADV-IMU measurements (black), and an ADP on the anchor (red). Note that the vertical scale on the three axes vary by an order of magnitude; the small ticks in A and B are equivalent to the ticks in C.	42
702	<b>Fig. 9.</b>	Turbulence spectra from the June 2014 TTM deployment. Each column is for a range of streamwise velocity magnitudes (indicated at top, in $\text{m s}^{-1}$ ). The rows are for each component of velocity (indicated at far right). The uncorrected spectra are black, the corrected spectra are blue, and the spectra of ADV head motion is red (also indicated in the legend). The vertical red dotted line indicates $f_a$ for estimating $\mathbf{u}_h$ ; below this frequency $S\{\mathbf{u}_h\}$ is plotted as a dashed line. Diagonal black dotted lines indicate a $f^{-5/3}$ slope. The cyan line in the first and last rows indicates the semi-empirical Kaimal spectrum for the measured values of $u_*$ and $\bar{U}$ . The number of spectral ensembles, $N$ , in each column is indicated in the top row.	43

711	<b>Fig. 10.</b> Turbulence spectra from the SMB. The axes layout and annotations are identical to Figure 9, except that $S\{\mathbf{u}_h\}$ is plotted as a solid line at all frequencies because it is measured at all frequencies. . . . .	44
714	<b>Fig. 11.</b> Turbulence spectra from the turbulence torpedo during a 35-minute period when the mean velocity was $1.3 \text{ m s}^{-1}$ . Annotations and line colors are identical to Figure 9. . . . .	45
716	<b>Fig. 12.</b> Variance preserving cross-spectra between components of $\mathbf{u}$ (blue), $\mathbf{u}_h$ (red), and $\mathbf{u}_m$ (black) from the June 2014 TTM deployment. The upper row is $fC\{u, v\}$ , the middle row is $fC\{u, w\}$ , and the bottom row is $fC\{v, w\}$ (also indicated at right). Note that these cross-spectra are between components of a velocity vector (e.g., $\mathbf{u}$ ), not between different vectors (i.e., not between $\mathbf{u}$ and $\mathbf{u}_m$ ). $N$ is the number of spectral ensembles in this average, i.e. when $2 <  u  < 2.5 \text{ ms}^{-1}$ . The light blue shading indicates one standard deviation of $fC\{\mathbf{u}\}$ . . . . .	46
723	<b>Fig. 13.</b> Non-dimensional cross-spectra of motion corrected velocity, $\hat{C}\{u, w\}$ , on a log-log scale. The average over $\Delta\hat{f} = 0.04$ bins is shown in blue, and single points are grey (negative values not shown). The semi-empirical Kaimal et al. (1972) form is shown as a thick black line, and the red dashed line indicates a $\hat{f}^{-7/3}$ slope. Cross-spectral estimates from measurements from a fixed ‘tripod’ are in purple. . . . .	47
727	<b>Fig. 14.</b> Time series of mean velocities (A), turbulence energy and its components (B), Reynold’s stresses (C), and turbulence dissipation rate (D) measured by the TTM during the June 2014 deployment. Shading indicates periods of ebb ( $\bar{u} > 1.0 \text{ ms}^{-1}$ , grey) and flood ( $\bar{u} < -1.0 \text{ ms}^{-1}$ , lighter grey). . . . .	48
731	<b>Fig. 15.</b> $P_{uz}$ vs. $\epsilon$ during the June 2014 TTM deployment for values of $ u  > 1 \text{ m/s}$ . Values of negative production are indicated as open circles. . . . .	49
733	<b>Fig. 16.</b> A log-log plot of $\epsilon$ vs. $\bar{U}$ for the June 2014 TTM (diamonds) and May 2015 SMB (dots) deployments, during ebb (left) and flood (right). Black points are 5-minute averages. Green dots are mean values within speed bins of $0.2 \text{ m s}^{-1}$ width that have at least 10 points (50 minutes of data); their vertical bars are 95% bootstrap confidence intervals. The blue line shows a $\bar{U}^3$ slope, wherein the proportionality constant (blue box) is calculated by taking the log-space mean of $\epsilon/\bar{U}^3$ . . . . .	50



739 FIG. 1. Bathymetry of Admiralty Inlet near Port Townsend, Washington, U.S.A. (Finlayson 2005). The red  
 740 dot indicates the location of all measurements. The positive  $u$  direction is the direction of ebb flow (thick arrow  
 741 originating from red dot), and positive  $v$  is away from Admiralty Head (smaller arrow).



742 FIG. 2. Schematic diagram of the TTM; not to scale. A pop-up buoy for anchor recovery is not shown, for  
743 simplicity.



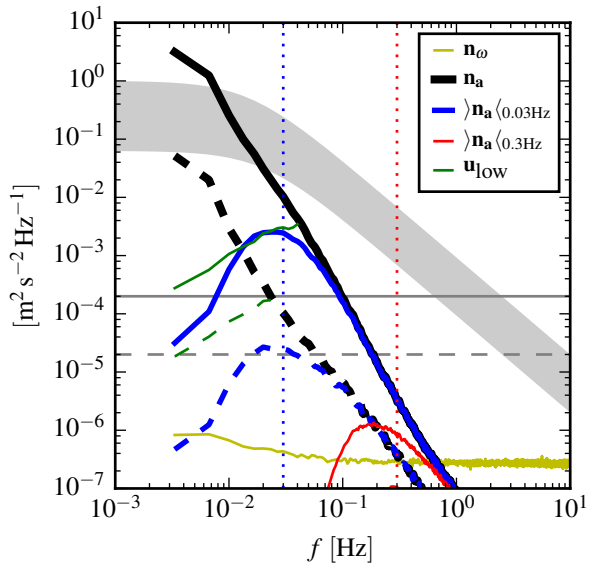
744 FIG. 3. TTM components on the deck of the R/V Jack Robertson. The TTM includes two ADVs, with  
745 pressure cases mounted on opposite sides of the fin. The anchor stack includes a pop-up buoy for retrieval. The  
746 green arrow indicates the vector from the IMU to the ADV head (face of the transmit transducer).



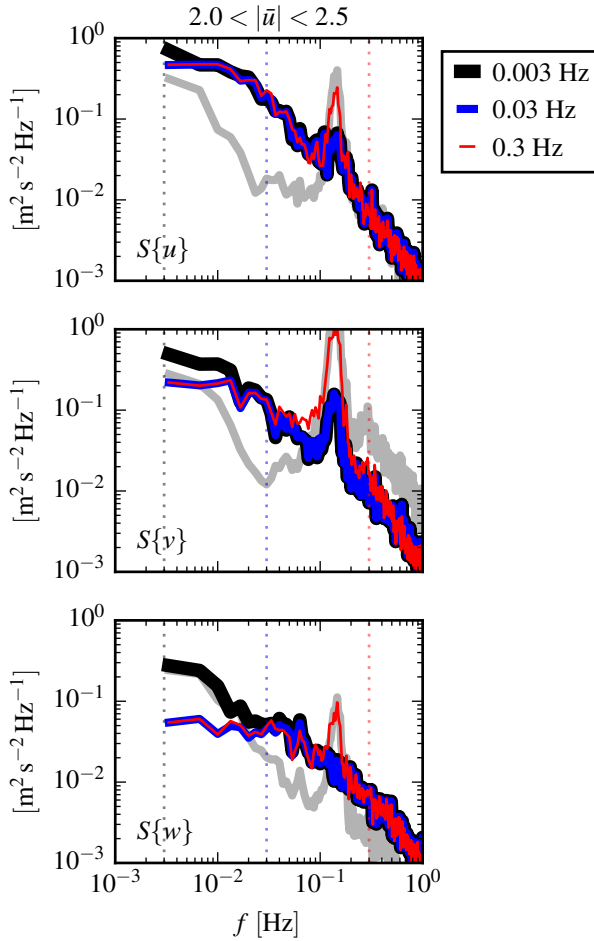
747 FIG. 4. Top: Alex DeKlerk checks to ensure that the SMB buoy is properly fastened to its anchor; the  
 748 RDI workhorse ADP can be seen in the rear instrument bay. A bridle is draped across the top of the buoy for  
 749 deployment and recovery, and a small marker buoy fastened to the tail is useful during recovery. Bottom: a  
 750 close-up of the SMB buoy with the ADV head and the top of its pressure case. The green arrow indicates the  
 751 vector from the IMU to the ADV head.



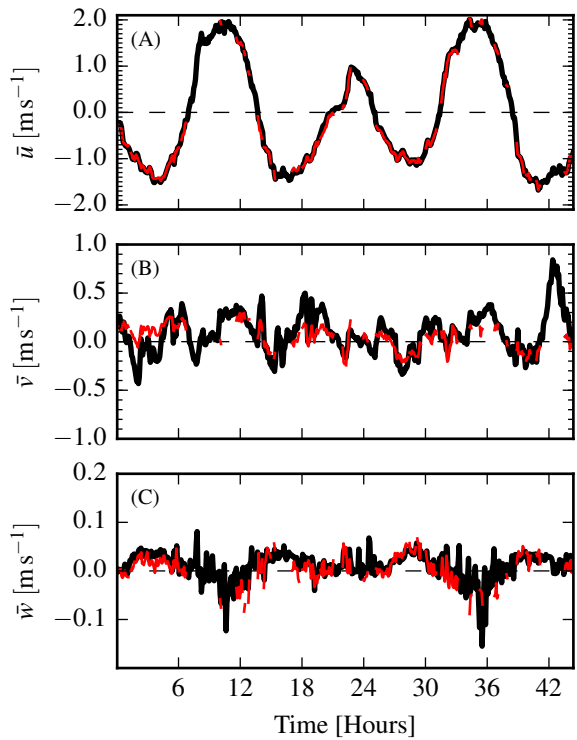
752 FIG. 5. The turbulence platform showing details of the ADV head and pressure case configuration. The green  
753 arrow indicates the vector from the IMU to the ADV head. The head cable was taped out of the way beneath the  
754 sounding weight tail fins shortly after taking this photo.



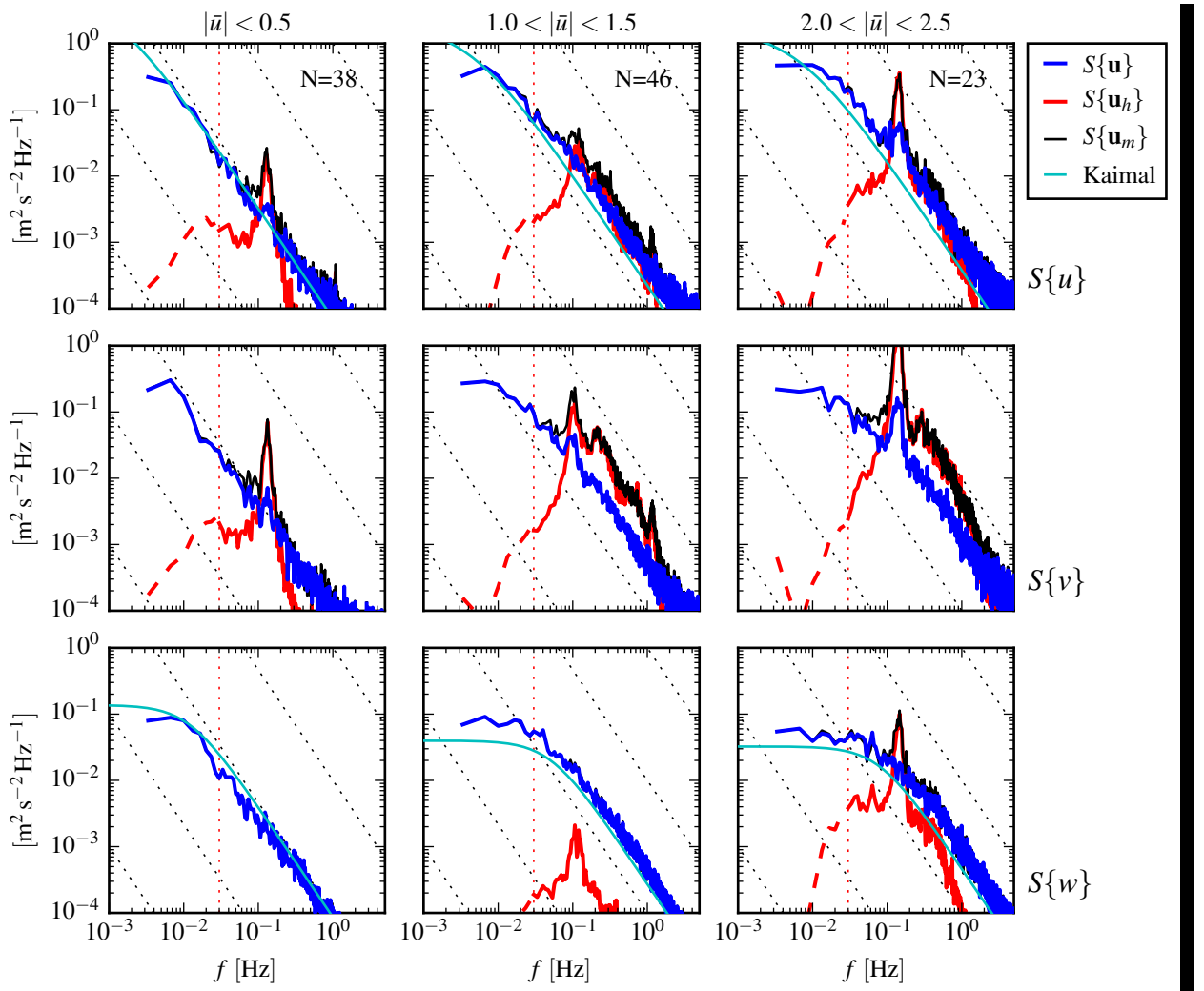
755 FIG. 6. The spectral noise levels of rotational velocity ( $S\{n_\omega\}$ , yellow) and translational velocity ( $S\{n_a\}$ ,  
 756 black) estimated from an ADV-IMU resting motionless on a table. Solid and dashed lines indicate the horizontal  
 757 and vertical components, respectively, of  $S\{n_a\}$  and  $S\{u_{low}\}$ . The  $n_a$  signals are unfiltered (black), and high-  
 758 pass filtered at 0.03 Hz (blue) and 0.3 Hz (red); vertical dotted lines indicate the filter frequency. Green lines are  
 759 an estimate of  $u_{low}$  for the TTM. Grey horizontal lines indicate the horizontal (solid) and vertical (dashed) ADV  
 760 noise levels. The shaded region indicates the range of  $S\{u\}$  presented in the next section.



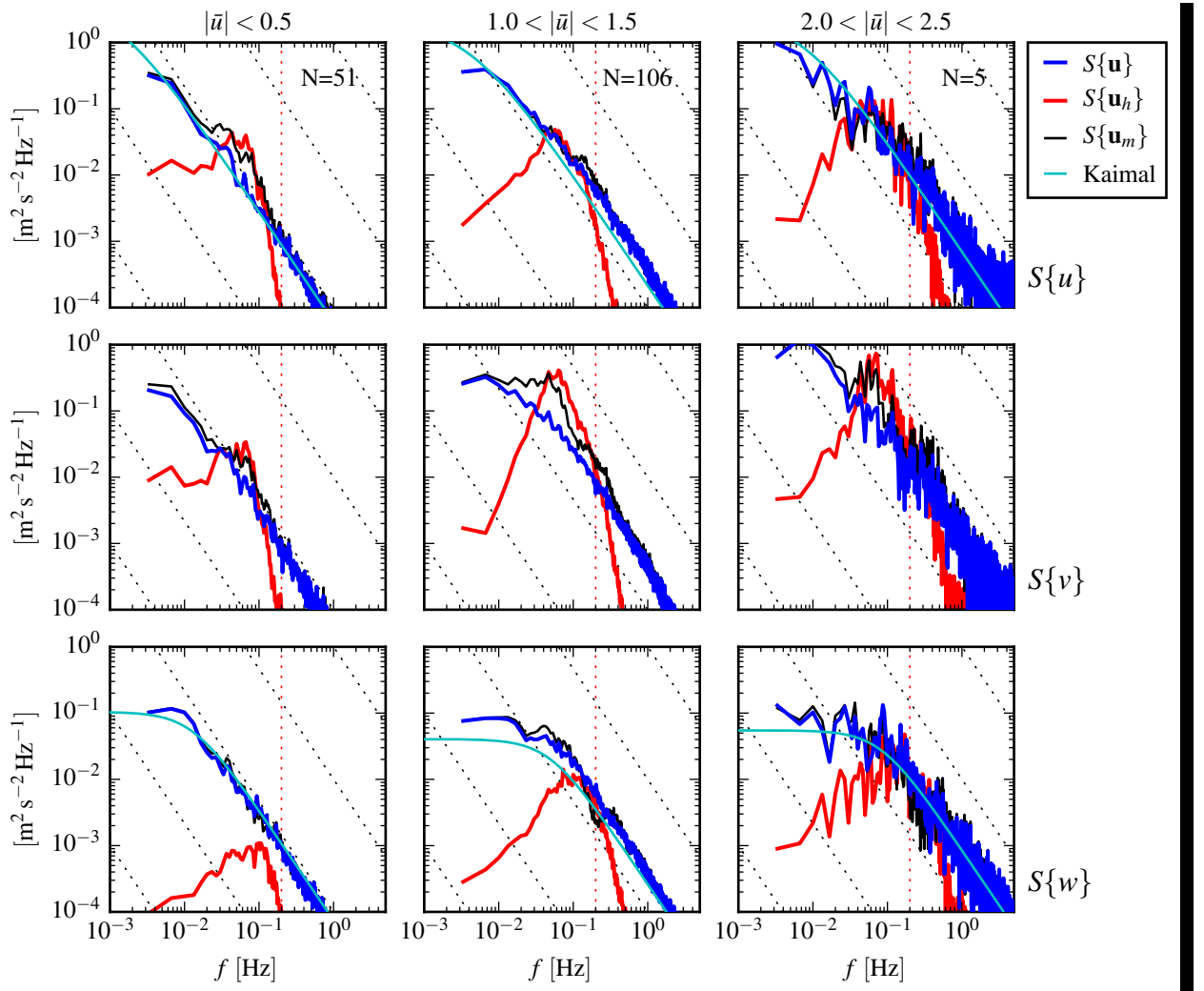
761 FIG. 7. Motion-corrected velocity spectra,  $S\{\mathbf{u}\}$ , for a range of high-pass filter frequencies:  $f_a = 0.3$  Hz  
 762 (thin red), 0.03 Hz (blue), and 0.003 Hz (thick black). The vertical dotted lines indicate the filter frequency.  
 763 The thick grey line is  $S\{\mathbf{u}_h\}$  for  $f_a = 0.003$  Hz. The data are from the June 2014 TTM deployment when  
 764  $2.0 < |\bar{u}| < 2.5 \text{ ms}^{-1}$ .



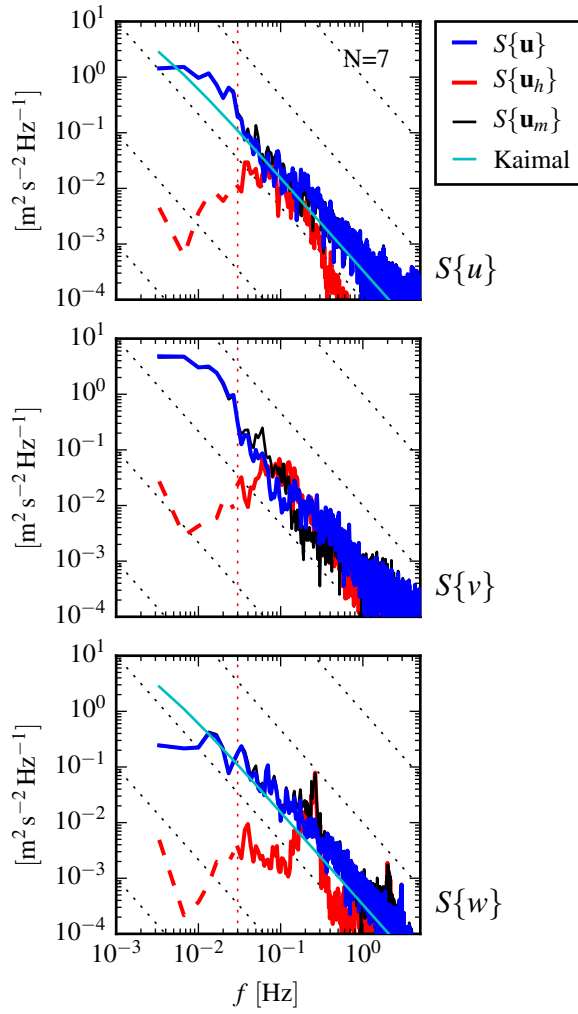
765 FIG. 8. Time series of tidal velocity in June 2012 at Admiralty Head from ADV-IMU measurements (black),  
 766 and an ADP on the anchor (red). Note that the vertical scale on the three axes vary by an order of magnitude;  
 767 the small ticks in A and B are equivalent to the ticks in C.



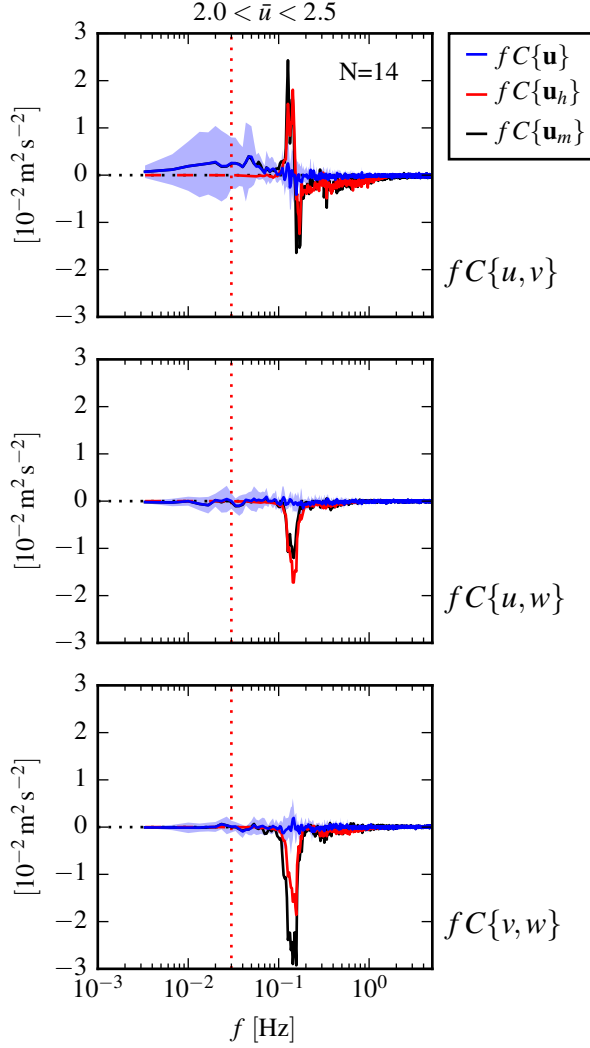
768 FIG. 9. Turbulence spectra from the June 2014 TTM deployment. Each column is for a range of streamwise  
 769 velocity magnitudes (indicated at top, in  $\text{m s}^{-1}$ ). The rows are for each component of velocity (indicated at far  
 770 right). The uncorrected spectra are black, the corrected spectra are blue, and the spectra of ADV head motion is  
 771 red (also indicated in the legend). The vertical red dotted line indicates  $f_a$  for estimating  $\mathbf{u}_h$ ; below this frequency  
 772  $S\{\mathbf{u}_h\}$  is plotted as a dashed line. Diagonal black dotted lines indicate a  $f^{-5/3}$  slope. The cyan line in the first  
 773 and last rows indicates the semi-empirical Kaimal spectrum for the measured values of  $u_*$  and  $\bar{U}$ . The number  
 774 of spectral ensembles,  $N$ , in each column is indicated in the top row.



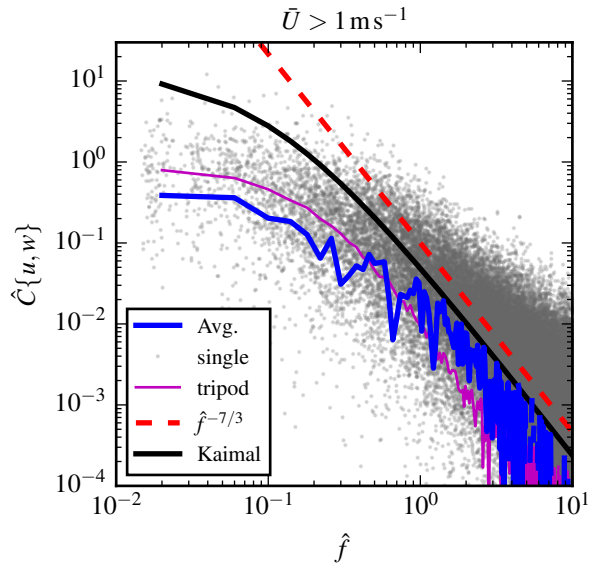
775 FIG. 10. Turbulence spectra from the SMB. The axes layout and annotations are identical to Figure 9, except  
 776 that  $S\{\mathbf{u}_h\}$  is plotted as a solid line at all frequencies because it is measured at all frequencies.



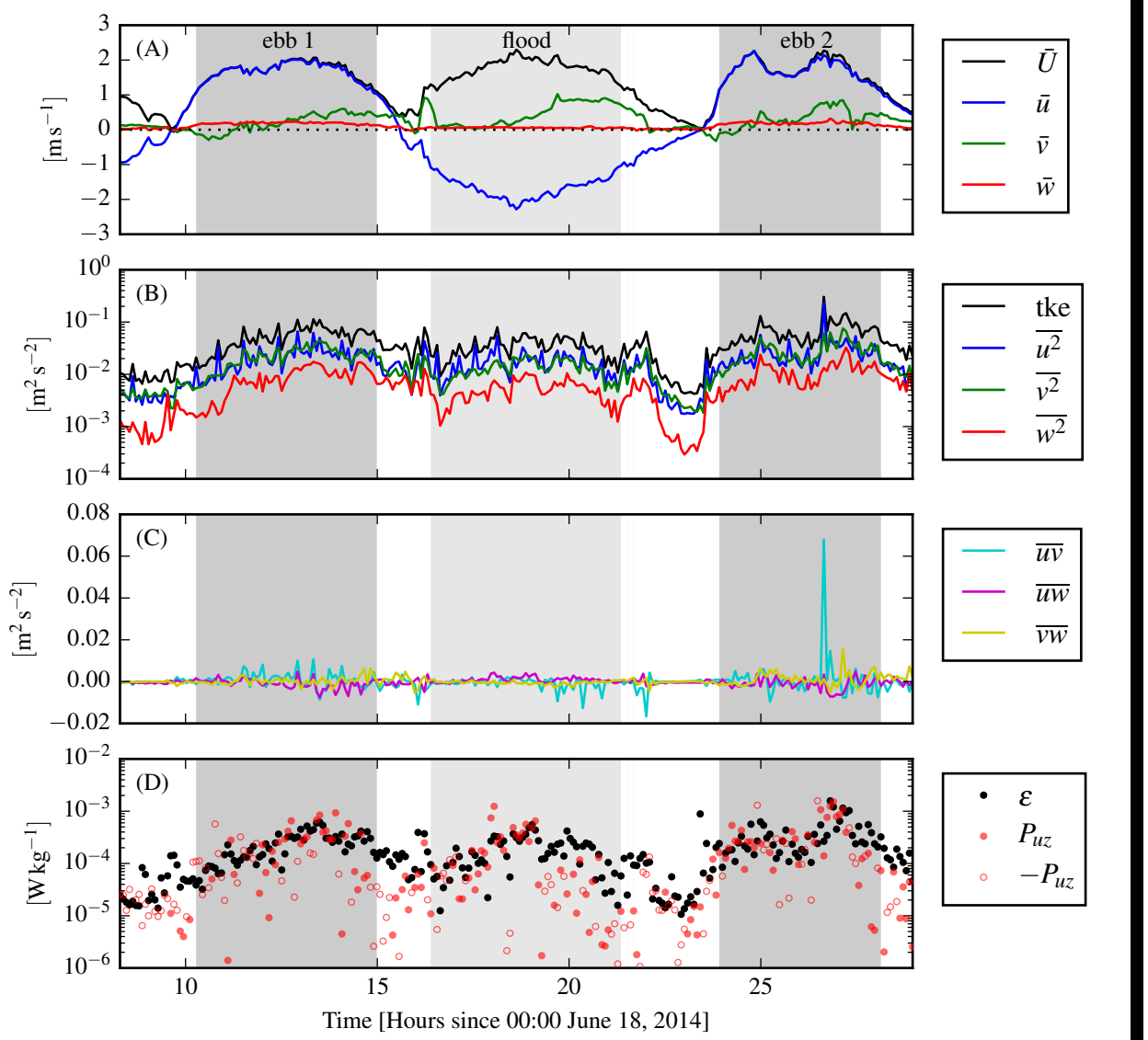
777 FIG. 11. Turbulence spectra from the turbulence torpedo during a 35-minute period when the mean velocity  
 778 was  $1.3 \text{ m s}^{-1}$ . Annotations and line colors are identical to Figure 9.



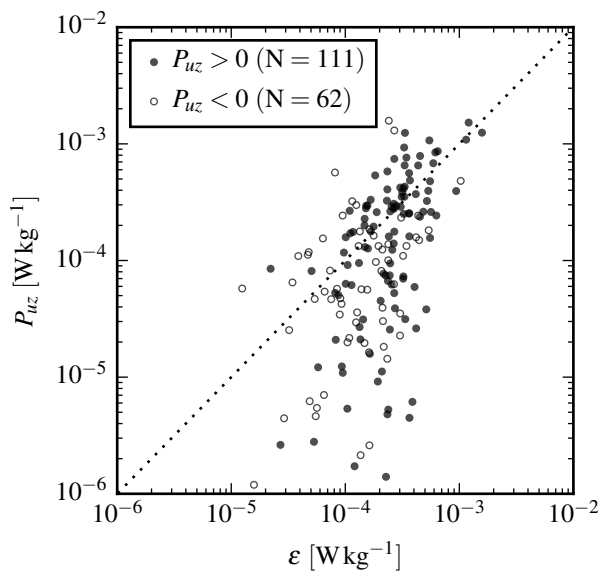
779 FIG. 12. Variance preserving cross-spectra between components of  $\mathbf{u}$  (blue),  $\mathbf{u}_h$  (red), and  $\mathbf{u}_m$  (black) from  
 780 the June 2014 TTM deployment. The upper row is  $fC\{\mathbf{u}, \mathbf{v}\}$ , the middle row is  $fC\{\mathbf{u}, \mathbf{w}\}$ , and the bottom row  
 781 is  $fC\{\mathbf{v}, \mathbf{w}\}$  (also indicated at right). Note that these cross-spectra are between components of a velocity vector  
 782 (e.g.,  $\mathbf{u}$ ), not between different vectors (i.e., not between  $\mathbf{u}$  and  $\mathbf{u}_m$ ).  $N$  is the number of spectral ensembles in  
 783 this average, i.e. when  $2 < |\mathbf{u}| < 2.5 \text{ m s}^{-1}$ . The light blue shading indicates one standard deviation of  $fC\{\mathbf{u}\}$ .



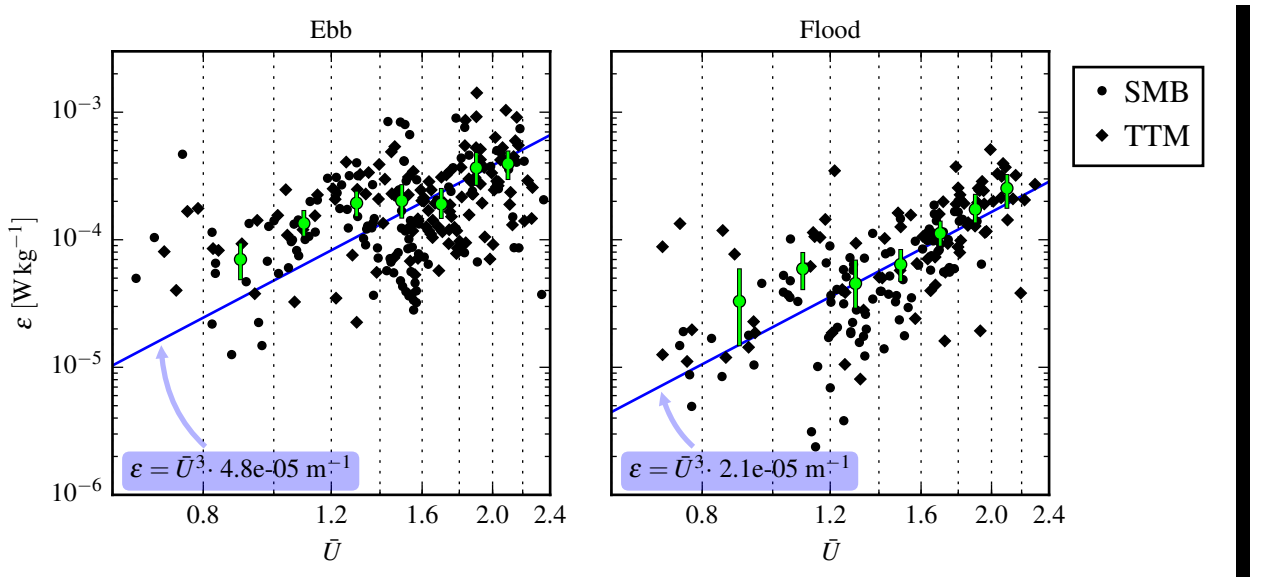
784 FIG. 13. Non-dimensional cross-spectra of motion corrected velocity,  $\hat{C}\{u, w\}$ , on a log-log scale. The average  
 785 over  $\Delta \hat{f} = 0.04$  bins is shown in blue, and single points are grey (negative values not shown). The semi-empirical  
 786 Kaimal et al. (1972) form is shown as a thick black line, and the red dashed line indicates a  $\hat{f}^{-7/3}$  slope. Cross-  
 787 spectral estimates from measurements from a fixed ‘tripod’ are in purple.



788 FIG. 14. Time series of mean velocities (A), turbulence energy and its components (B),  
 789 Reynold's stresses (C), and turbulence dissipation rate (D) measured by the TTM during the June 2014 deployment. Shading indicates  
 790 periods of ebb ( $\bar{u} > 1.0 \text{ ms}^{-1}$ , grey) and flood ( $\bar{u} < -1.0 \text{ ms}^{-1}$ , lighter grey).



791 FIG. 15.  $P_{uz}$  vs.  $\epsilon$  during the June 2014 TTM deployment for values of  $|u| > 1$  m/s. Values of negative  
792 production are indicated as open circles.



793 FIG. 16. A log-log plot of  $\varepsilon$  vs.  $\bar{U}$  for the June 2014 TTM (diamonds) and May 2015 SMB (dots) deployments,  
 794 during ebb (left) and flood (right). Black points are 5-minute averages. Green dots are mean values within  
 795 speed bins of  $0.2 \text{ m s}^{-1}$  width that have at least 10 points (50 minutes of data); their vertical bars are 95%  
 796 bootstrap confidence intervals. The blue line shows a  $\bar{U}^3$  slope, wherein the proportionality constant (blue box)  
 797 is calculated by taking the log-space mean of  $\varepsilon/\bar{U}^3$ .